

Waveguide Excited Microstrip Patch Antenna—Theory and Experiment

Min-Hua Ho, *Member, IEEE*, Krzysztof A. Michalski, *Senior Member, IEEE*, and Kai Chang, *Fellow, IEEE*

Abstract—An arbitrarily shaped microstrip patch antenna excited through an arbitrarily shaped aperture in the mouth of a rectangular waveguide is investigated theoretically and experimentally. The metallic patch resides on a dielectric substrate grounded by the waveguide flange and may be covered by a dielectric superstrate. The substrate (and superstrate, if present) consists of one or more planar, homogeneous layers, which may exhibit uniaxial anisotropy. The analysis is based on the space domain integral equation approach. More specifically, the Green's functions for the layered medium and the waveguide are used to formulate a coupled set of integral equations for the patch current and the aperture electric field. The layered medium Green's function is expressed in terms of Sommerfeld-type integrals and the waveguide Green's function in terms of Floquet series, which are both accelerated to reduce the computational effort. The coupled integral equations are solved by the method of moments using vector basis functions defined over triangular subdomains. The dominant mode reflection coefficient in the waveguide and the far-field radiation patterns are then found from the computed aperture field and patch current distributions. The radar cross section (RCS) of a plane-wave excited structure is obtained in a like manner. Sample numerical results are presented and are found to be in good agreement with measurements and with published data.

I. INTRODUCTION

MICROSTRIP patch antennas, which belong to a large class of printed circuit antennas, are widely used in the microwave frequency range, both as single elements and (more often) in array configurations. Their advantages are well known: low cost, conformity, ease of fabrication and integration, reproducibility, ruggedness, light weight, and low profile [1], [2]. In recent years, the utilization of millimeter-wave systems, with smaller, lighter components and antennas, has provided a wider bandwidth, and consequently higher data rate communication and better resolution than microwave systems [3], [4]. However, the feed structures that operate well at microwave frequencies are not always viable in the millimeter-wave range. For example, microstrip line losses become significant and coaxial feed components are not available above about 50 GHz, which renders the direct feed techniques impractical in this frequency range. On the other hand, the indirect waveguide feed becomes an attractive option for millimeter-wave antennas and antenna arrays [5] because the waveguide bulkiness becomes less of a factor, while its losses

remain smaller than those of a microstrip line [6]. Moreover, in some applications the aluminum waveguide may also serve as a heat sink and support for active devices that may be integrated with the antenna. Another antenna configuration that possesses the advantages listed above is a waveguide-fed slot antenna. Its gain, however, is significantly lower than that of a waveguide-excited microstrip patch.

In this paper, we present a rigorous integral equation analysis of a waveguide-fed microstrip patch antenna, as illustrated in Fig. 1. The arbitrarily shaped microstrip patch is coupled to the rectangular waveguide through an aperture, which may also be of arbitrary shape. The dielectric medium above the ground plane may consist of one or more planar, homogeneous layers, which may exhibit uniaxial anisotropy. The n th layer is characterized by the permittivity and permeability dyadics

$$\underline{\underline{\epsilon}}_n = \underline{\underline{I}}_t \epsilon_{tn} + \hat{z} \hat{z} \epsilon_{zn} \quad \underline{\underline{\mu}}_n = \underline{\underline{I}}_t \mu_{tn} + \hat{z} \hat{z} \mu_{zn} \quad (1)$$

where $\underline{\underline{I}}_t$ is the unit dyadic transverse to z , and ϵ_{tn} (μ_{tn}) and ϵ_{zn} (μ_{zn}) denote, respectively, the transverse and longitudinal dielectric (magnetic) constants relative to free space. (Observe that we distinguish dyadics by double underlines and unit vectors by carets.) The free-space permeability and permittivity will be denoted by μ_o and ϵ_o , respectively. For each layer, we also introduce its electric and magnetic anisotropy ratios, ν_n^e and ν_n^h , respectively, given as

$$\nu_n^e = \frac{\epsilon_{zn}}{\epsilon_{tn}}, \quad \nu_n^h = \frac{\mu_{zn}}{\mu_{tn}}. \quad (2)$$

The structure is excited either by the dominant (TE₁₀) waveguide mode or by a plane wave incident in the upper-half space. The primary quantities to be computed are the aperture field and patch current distributions. From these, other quantities of interest will be found, including the dominant mode reflection coefficient, the far-field radiation patterns, and the radar cross section (RCS). Although attention is limited to a single antenna element, it is expected that the results of this study will also be useful in the analysis, by an approximate technique, of finite waveguide-fed antenna arrays.

The remainder of this paper is organized as follows. In Section II, coupled integral equations are formulated for the patch current and the aperture electric field, where the latter is represented by an equivalent magnetic current. The kernels of these integral equations are expressed in terms of the voltage and current Green's functions of a transmission line network analog of the layered medium, which is discussed in Appendix I. In Section III, numerical procedures for the solution of the integral equations are described, with some auxiliary

Manuscript received June 2, 1993; revised January 28, 1994. This work was supported in part by the Office of Naval Research under Contract N00014-10-J-1197.

The authors are with the Electromagnetics and Microwave Laboratory, Department of Electrical Engineering, Texas A&M University, College Station, TX 77843-3128 USA.

IEEE Log Number 9403657.

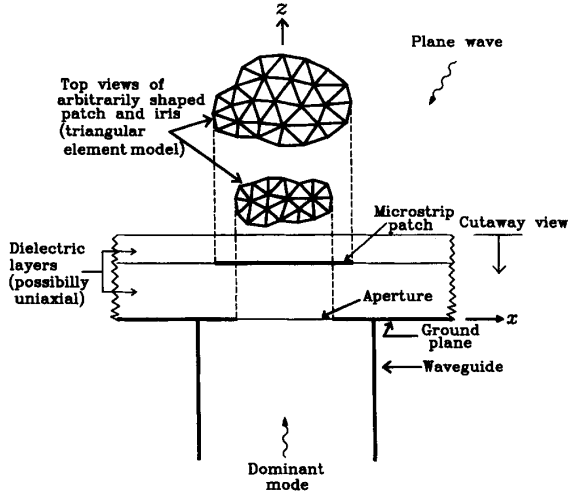


Fig. 1. Geometry of a waveguide-fed microstrip patch antenna.

developments relegated to Appendix II. Sample computed and measured results are given in Section IV, and conclusions are stated in Section V.

II. FORMULATION

A. Integral Equations

To facilitate the analysis of the structure shown in Fig. 1, we invoke the equivalence principle [7] to in effect decouple the original problem into two simpler ones, referred to as the *interior* (inside the shorted waveguide) and *exterior* (above the ground plane) problems, as illustrated in Fig. 2. This decoupling is achieved by first shorting the aperture S_a through which the two regions interact, and then placing over it an equivalent magnetic current \mathbf{M}_S , which represents the tangential electric field in the aperture. The negative of \mathbf{M}_S is placed on the opposite side of the shorted aperture, thus explicitly enforcing the continuity of the tangential electric field across S_a . In the equivalent problem, the effect of the metallic patch S_p (which is assumed to be perfectly conducting) is replaced by an equivalent electric current \mathbf{J}_S , representing the vector sum of the surface currents on both sides of the patch.

The conditions of vanishing tangential electric field on the patch and continuity of the tangential magnetic field across the aperture may now be stated as

$$-\hat{\mathbf{z}} \times \mathbf{E}_+^s(\mathbf{r}) = \hat{\mathbf{z}} \times \mathbf{E}_+^i(\mathbf{r}), \quad \mathbf{r} \in S_p, \quad (3)$$

$$-\hat{\mathbf{z}} \times [\mathbf{H}_+^s(\mathbf{r}) - \mathbf{H}_-^s(\mathbf{r})] = \hat{\mathbf{z}} \times [\mathbf{H}_+^i(\mathbf{r}) - \mathbf{H}_-^i(\mathbf{r})], \quad \mathbf{r} \in S_a \quad (4)$$

where the subscripts + and - refer to, respectively, the exterior and the interior regions, \mathbf{r} is a position vector with respect to the global coordinate origin, $(\mathbf{E}^i, \mathbf{H}^i)$ are the short-circuit electric and magnetic fields of known sources, computed in the absence of the patch and with the aperture

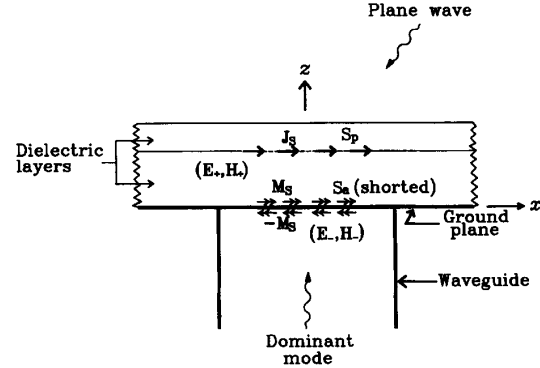


Fig. 2. Problem equivalent to that in Fig. 1.

shorted [8], and $(\mathbf{E}^s, \mathbf{H}^s)$ are the scattered fields produced by \mathbf{J}_S and \mathbf{M}_S . The scattered fields in (3) and (4) can be expressed in terms of the dyadic and scalar kernels of the exterior and interior problems as [9]

$$\begin{aligned} \mathbf{E}_+^s(\mathbf{r}) = & - \int_{S_p} \underline{\underline{\mathbf{G}}}^A(\mathbf{r} | \mathbf{r}') \cdot \mathbf{J}_S(\boldsymbol{\rho}') dS' \\ & - \nabla \int_{S_p} G^\phi(\mathbf{r} | \mathbf{r}') \nabla' \cdot \mathbf{J}_S(\boldsymbol{\rho}') dS' \\ & + \int_{S_a} \underline{\underline{\mathbf{G}}}^{\text{EM}}(\mathbf{r} | \mathbf{r}') \cdot \mathbf{M}_S(\boldsymbol{\rho}') dS', \end{aligned} \quad (5)$$

$$\begin{aligned} \mathbf{H}_+^s(\mathbf{r}) = & \int_{S_p} \underline{\underline{\mathbf{G}}}^{\text{HJ}}(\mathbf{r} | \mathbf{r}') \cdot \mathbf{J}_S(\boldsymbol{\rho}') dS' \\ & - \int_{S_a} \underline{\underline{\mathbf{G}}}^{F+}(\mathbf{r} | \mathbf{r}') \cdot \mathbf{M}_S(\boldsymbol{\rho}') dS' \\ & - \nabla \int_{S_a} G^{\vartheta+}(\mathbf{r} | \mathbf{r}') \nabla' \cdot \mathbf{M}_S(\boldsymbol{\rho}') dS', \end{aligned} \quad (6)$$

$$\begin{aligned} \mathbf{H}_-^s(\mathbf{r}) = & \int_{S_a} \underline{\underline{\mathbf{G}}}^{F-}(\mathbf{r} | \mathbf{r}') \cdot \mathbf{M}_S(\boldsymbol{\rho}') dS' \\ & + \nabla \int_{S_a} G^{\vartheta-}(\mathbf{r} | \mathbf{r}') \nabla' \cdot \mathbf{M}_S(\boldsymbol{\rho}') dS' \end{aligned} \quad (7)$$

where primes indicate source coordinates and $\boldsymbol{\rho}$ is the projection of \mathbf{r} on the x - y plane. Upon substituting (5)–(7) into (3)–(4), we obtain a coupled set of integral equations for the unknown equivalent currents \mathbf{J}_S and \mathbf{M}_S , given as

$$\begin{aligned} \langle \underline{\underline{\mathbf{G}}}_t^A; \mathbf{J}_S \rangle'_{S_p} + \nabla_t \langle G^\phi; \nabla_t' \cdot \mathbf{J}_S \rangle'_{S_p} \\ - \langle \underline{\underline{\mathbf{G}}}_t^{\text{EM}}; \mathbf{M}_S \rangle'_{S_a} = \mathbf{E}_{t,+}^i(\mathbf{r}), \quad \mathbf{r} \in S_p, \end{aligned} \quad (8)$$

$$\begin{aligned} \langle \underline{\underline{\mathbf{G}}}_t^{\text{HJ}}; \mathbf{J}_S \rangle'_{S_p} - \langle \underline{\underline{\mathbf{G}}}_t^{F+} + \underline{\underline{\mathbf{G}}}_t^{F-}; \mathbf{M}_S \rangle'_{S_a} \\ - \nabla_t \langle G^{\vartheta+} + G^{\vartheta-}; \nabla_t' \cdot \mathbf{M}_S \rangle'_{S_a} \\ = \mathbf{H}_{t,+}^i(\mathbf{r}) - \mathbf{H}_{t,-}^i(\mathbf{r}), \quad \mathbf{r} \in S_a. \end{aligned} \quad (9)$$

Here, we have introduced the notation $\langle \cdot, \cdot \rangle$ for an integral of a product of two functions separated by the comma. The dot over the comma signifies a *dot product* of vector arguments, while the prime over \rangle indicates that the integration is over the primed coordinates. Further, the subscript t distinguishes

components transverse to $\hat{\mathbf{z}}$, and the subscripts S_p and S_a indicate the integration domains (see Fig. 2). The dyadic kernels in (8) and (9) are given as [9]

$$\underline{\underline{\mathbf{G}}}_t^A(\mathbf{r} | \mathbf{r}') = \underline{\underline{\mathbf{I}}}_t G_{xx}^A(\mathbf{r} | \mathbf{r}'), \quad (10)$$

$$\underline{\underline{\mathbf{G}}}_t^{\text{EM}}(\mathbf{r} | \mathbf{r}') = (\hat{\mathbf{x}}\hat{\mathbf{x}} - \hat{\mathbf{y}}\hat{\mathbf{y}})G_{xx}^{\text{EM}}(\mathbf{r} | \mathbf{r}') + \hat{\mathbf{x}}\hat{\mathbf{y}}G_{xy}^{\text{EM}}(\mathbf{r} | \mathbf{r}') + \hat{\mathbf{y}}\hat{\mathbf{x}}G_{yx}^{\text{EM}}(\mathbf{r} | \mathbf{r}'), \quad (11)$$

$$\underline{\underline{\mathbf{G}}}_t^{\text{HJ}}(\mathbf{r} | \mathbf{r}') = (-\hat{\mathbf{x}}\hat{\mathbf{x}} + \hat{\mathbf{y}}\hat{\mathbf{y}})G_{xx}^{\text{EM}}(\mathbf{r}' | \mathbf{r}) - \hat{\mathbf{x}}\hat{\mathbf{y}}G_{yx}^{\text{EM}}(\mathbf{r}' | \mathbf{r}) - \hat{\mathbf{y}}\hat{\mathbf{x}}G_{xy}^{\text{EM}}(\mathbf{r}' | \mathbf{r}), \quad (12)$$

$$\underline{\underline{\mathbf{G}}}_t^{F+}(\mathbf{r} | \mathbf{r}') = \underline{\underline{\mathbf{I}}}_t G_{xx}^{F+}(\mathbf{r} | \mathbf{r}'), \quad (13)$$

$$\underline{\underline{\mathbf{G}}}_t^{F-}(\mathbf{r} | \mathbf{r}') = \hat{\mathbf{x}}\hat{\mathbf{x}}G_{xx}^{F-}(\mathbf{r} | \mathbf{r}') + \hat{\mathbf{y}}\hat{\mathbf{y}}G_{yy}^{F-}(\mathbf{r} | \mathbf{r}') \quad (14)$$

where

$$G_{xx}^A(\mathbf{r} | \mathbf{r}') = S_0 \{V_i^h(k_\rho; z | z')\}, \quad (15)$$

$$G_{xx}^{\text{EM}}(\mathbf{r} | \mathbf{r}') = -\frac{\sin 2\zeta}{2} S_2 \left\{ \frac{V_v^e(k_\rho; z | z') - V_v^h(k_\rho; z | z')}{k_\rho^2} \right\}, \quad (16)$$

$$G_{xy}^{\text{EM}}(\mathbf{r} | \mathbf{r}') = \frac{\cos 2\zeta}{2} S_2 \left\{ \frac{V_v^e(k_\rho; z | z') - V_v^h(k_\rho; z | z')}{k_\rho^2} \right\} + \frac{1}{2} S_0 \{V_v^e(k_\rho; z | z') + V_v^h(k_\rho; z | z')\}, \quad (17)$$

$$G_{yx}^{\text{EM}}(\mathbf{r} | \mathbf{r}') = \frac{\cos 2\zeta}{2} S_2 \left\{ \frac{V_v^e(k_\rho; z | z') - V_v^h(k_\rho; z | z')}{k_\rho^2} \right\} - \frac{1}{2} S_0 \{V_v^e(k_\rho; z | z') + V_v^h(k_\rho; z | z')\}, \quad (18)$$

$$G_{xx}^{F+}(\mathbf{r} | \mathbf{r}') = S_0 \{I_v^e(k_\rho; z | z')\}, \quad (19)$$

$$G_{xx}^{F-}(\mathbf{r} | \mathbf{r}') = \left[\mathcal{F}_{mn}^{(z')} - \mathcal{F}_{mn}^{(a-z')} - \mathcal{F}_{mn}^{(b-z')} + \mathcal{F}_{mn}^{(b-z')} \right] \times \{I_v^e(k_\rho; z | z')\}, \quad (20)$$

$$G_{yy}^{F-}(\mathbf{r} | \mathbf{r}') = \left[\mathcal{F}_{mn}^{(z')} + \mathcal{F}_{mn}^{(a-z')} - \mathcal{F}_{mn}^{(b-z')} - \mathcal{F}_{mn}^{(b-z')} \right] \times \{I_v^e(k_\rho; z | z')\} \quad (21)$$

and the scalar kernels are given as

$$G^\phi(\mathbf{r} | \mathbf{r}') = S_0 \left\{ \frac{V_i^h(k_\rho; z | z') - V_i^e(k_\rho; z | z')}{k_\rho^2} \right\}, \quad (22)$$

$$G^{\theta+}(\mathbf{r} | \mathbf{r}') = S_0 \left\{ \frac{I_v^e(k_\rho; z | z') - I_v^h(k_\rho; z | z')}{k_\rho^2} \right\}, \quad (23)$$

$$G^{\theta-}(\mathbf{r} | \mathbf{r}') = \left[\mathcal{F}_{mn}^{(z')} + \mathcal{F}_{mn}^{(a-z')} + \mathcal{F}_{mn}^{(b-z')} + \mathcal{F}_{mn}^{(b-z')} \right] \times \left\{ \frac{I_v^e(k_\rho; z | z') - I_v^h(k_\rho; z | z')}{k_\rho^2} \right\}. \quad (24)$$

In the above, we have introduced the Sommerfeld integral notation

$$S_n \{f(k_\rho)\} = \frac{1}{2\pi} \int_0^\infty f(k_\rho) J_n(k_\rho \xi) k_\rho^{n+1} dk_\rho, \quad n = 0, 1, 2, \quad (25)$$

$$\xi = \sqrt{(x-x')^2 + (y-y')^2}, \quad \zeta = \arctan \left(\frac{y-y'}{x-x'} \right) \quad (26)$$

where J_n is the Bessel function of order n , and the Floquet series notation

$$\mathcal{F}_{mn}^{(z')} \{f(k_\rho)\} = \frac{1}{A_w} \sum_{m=-\infty}^{+\infty} \sum_{n=-\infty}^{+\infty} f(k_{\rho mn}) \times e^{-j[\mathbf{k}_{\rho mn} \cdot (\boldsymbol{\rho} - \mathbf{x}'\hat{\mathbf{x}} - \mathbf{y}'\hat{\mathbf{y}})]} \quad (27)$$

with

$$\mathbf{k}_{\rho mn} = k_{xm} \hat{\mathbf{x}} + k_{yn} \hat{\mathbf{y}}, \quad k_{\rho mn} = \sqrt{k_{xm}^2 + k_{yn}^2}, \quad k_{xm} = \frac{m\pi}{d_x}, \quad k_{yn} = \frac{n\pi}{d_y}. \quad (28)$$

Here, $A_w = d_x d_y$, with $d_x = 2a$ and $d_y = 2b$, where a and b are the inner waveguide dimensions along the x and y directions, respectively. The symbols V_α^p and I_α^p in (15)–(24), where p stands for e (E mode) or h (H mode) and α stands for i (current source) or v (voltage source), denote, respectively, the voltage and current transmission-line Green's functions discussed in Appendix A. The four series in (20)–(21) and (24) arise from the multiple images of a transverse magnetic dipole in the walls of a rectangular waveguide.

Once the current distributions \mathbf{J}_S and \mathbf{M}_S are determined, the secondary quantities of interest, such as the waveguide dominant mode reflection coefficient at the aperture, the far-zone field radiation patterns, and the RCS can be found with little extra effort.

B. Short-Circuit Incident Fields

In the driven antenna analysis, the incident electric field in the air-filled waveguide is taken to be that of the dominant TE₁₀ mode (we assume that $a \geq b$), and is given as

$$\mathbf{E}_{-}^{\text{inc}}(\mathbf{r}) = V_o \mathbf{e}_{10}(\boldsymbol{\rho}) e^{-jk_{z10}z} \quad (29)$$

with

$$\mathbf{e}_{10}(\boldsymbol{\rho}) = \hat{\mathbf{y}} \sqrt{\frac{2}{ab}} \cos\left(\frac{\pi x}{a}\right), \quad k_{z10} = \sqrt{k_o^2 - \left(\frac{\pi}{a}\right)^2} \quad (30)$$

where $k_o = \sqrt{\mu_0 \epsilon_0}$ is the free-space wavenumber. This transverse component of the short-circuit magnetic field associated with this incident wave is given as

$$\mathbf{H}_{t,-}^i(\mathbf{r}) = Y_{10} V_o \mathbf{h}_{10} \left[1 - \bar{\Gamma}_{10}(z) \right] e^{-jk_{z10}z} \quad (31)$$

with

$$\mathbf{h}_{10}(\boldsymbol{\rho}) = \hat{\mathbf{z}} \times \mathbf{e}_{10}, \quad Y_{10} = \frac{k_{z10}}{k_o \eta_o} \quad (32)$$

where $\eta_o = \sqrt{\mu_o / \epsilon_o}$ is the free space intrinsic impedance. In (31), $\bar{\Gamma}_{10}(z)$ is the dominant mode reflection coefficient in the short-circuited waveguide.

In the RCS analysis, the structure is illuminated by a uniform plane wavefield

$$\mathbf{E}_{+}^{\text{inc}}(\mathbf{r}) = (\hat{\boldsymbol{\theta}}_i E_\theta^i + \hat{\boldsymbol{\phi}}_i E_\phi^i) e^{jk_o[\rho \sin \theta_i \cos(\varphi - \varphi_i) + (z-d) \cos \theta_i]} \quad (33)$$

impinging from the direction (θ_i, φ_i) in the upper half-space, which is assumed to have free-space parameters. Observe that in (33) the phase reference point is chosen at $(0, 0, d)$, where d is the z -coordinate of the uppermost interface. This plane wave is the source of the short-circuit electric field, whose transverse part is given as

$$\mathbf{E}_{t,+}^i(\mathbf{r}) = [\hat{\rho}_i V^e(k_\rho^i; z | d) + \hat{\varphi}_i V^h(k_\rho^i; z | d)] e^{j\mathbf{k}_\rho^i \cdot \boldsymbol{\rho}} \quad (34)$$

where $\mathbf{k}_\rho^i = \hat{\rho}_i k_\rho^i$, with $k_\rho^i = k_o \sin \theta_i$. In the above, $V^p(k_\rho^i; z | d)$ denotes the voltage on the respective transmission line analog of the layered medium, excited in the uppermost section by the voltage waves

$$V_-^e(k_\rho^i; z | d) = \cos \theta_i E_\theta^i e^{jk_o(z-d) \cos \theta_i} \quad (35)$$

$$V_-^h(k_\rho^i; z | d) = E_\varphi^i e^{jk_o(z-d) \cos \theta_i} \quad (36)$$

propagating in the $-z$ direction. The transverse component of the short-circuit magnetic field associated with (34) may be expressed as

$$\mathbf{H}_{t,+}^i(\mathbf{r}) = -[\hat{\rho}_i \mathbf{I}^h(k_\rho^i; z | d) - \hat{\varphi}_i \mathbf{I}^e(k_\rho^i; z | d)] e^{j\mathbf{k}_\rho^i \cdot \boldsymbol{\rho}}. \quad (37)$$

The voltages and currents in (34) and (37) can easily be found in any transmission line section, as discussed in Appendix I.

C. Secondary Quantities

From the equivalent currents \mathbf{J}_S and \mathbf{M}_S , other quantities of interest may easily be obtained. Hence, for the driven antenna we compute the dominant mode aperture reflection coefficient Γ and the corresponding normalized aperture admittance Y , given as [10]

$$\Gamma = -\frac{1}{V_o} \langle \mathbf{M}_S; \mathbf{h}_{10} \rangle_{S_a} - 1, \quad Y = \frac{1 - \Gamma}{1 + \Gamma} \quad (38)$$

For the plane-wave excited structure we also compute the dominant mode aperture transmission coefficient, given as

$$T = -\frac{\langle \mathbf{M}_S; \mathbf{h}_{10} \rangle_{S_a}}{\sqrt{|\cos \theta_i E_\theta^i|^2 + |E_\varphi^i|^2}}. \quad (39)$$

For either excitation, the far-zone fields in the direction (θ_o, φ_o) are obtained as

$$E_\theta^s \sim -\frac{jk_o}{2\pi r} e^{-jk_o(r-d \cos \theta_o)} \left\{ V_i^e(k_\rho^o; d | h) \hat{\rho}_o \cdot \left\langle \mathbf{J}_S(\boldsymbol{\rho}'), e^{j\mathbf{k}_\rho^o \cdot \boldsymbol{\rho}'} \right\rangle'_{S_p} + \eta_o \cos \theta_o I_v^e(k_\rho^o; d | 0) \hat{\varphi}_o \cdot \left\langle \mathbf{M}_S(\boldsymbol{\rho}'), e^{j\mathbf{k}_\rho^o \cdot \boldsymbol{\rho}'} \right\rangle'_{S_a} \right\}, \quad (40)$$

$$E_\varphi^s \sim -\frac{jk_o}{2\pi r} e^{-jk_o(r-d \cos \theta_o)} \left\{ \cos \theta_o V_i^h(k_\rho^o; d | h) \hat{\varphi}_o \cdot \left\langle \mathbf{J}_S(\boldsymbol{\rho}'), e^{j\mathbf{k}_\rho^o \cdot \boldsymbol{\rho}'} \right\rangle'_{S_p} - \eta_o I_v^h(k_\rho^o; d | 0) \hat{\rho}_o \cdot \left\langle \mathbf{M}_S(\boldsymbol{\rho}'), e^{j\mathbf{k}_\rho^o \cdot \boldsymbol{\rho}'} \right\rangle'_{S_a} \right\} \quad (41)$$

where $\hat{\rho}_o$ and $\hat{\varphi}_o$ are the radial and azimuthal unit vectors evaluated at (θ_o, φ_o) , and $\mathbf{k}_\rho^o = \hat{\rho}_o k_\rho^o$, with $k_\rho^o = k_o \sin \theta_o$. It

is assumed in (40) and (41) that the aperture is in the $z = 0$ plane and that the patch resides on a substrate with thickness h . Observe that (40) and (41) include contributions from both the patch and the aperture.

For the plane-wave excited antenna we also compute its monostatic RCS. Hence, if the incident field in the upper half-space is polarized in the u direction and the v component of the scattered field is considered, the RCS of the antenna is given as [9]

$$\sigma_{uv} = 4\pi r^2 \frac{|E_v^s|^2}{|E_{u,+}^{\text{inc}}|^2} \quad (42)$$

where $r \rightarrow \infty$. It should be noted that the scattered field in the above does not include the plane wave (geometrical optics) field reflected by the layered medium.

III. NUMERICAL PROCEDURE

A. Weak Form of the Integral Equations

The method of moments (MOM) is applied to the weak forms of (8) and (9), which are obtained by testing them with a set of suitably selected weight functions $\{\Lambda_m\}$ defined over S_p and S_a . As a result, upon using the Gauss theorem [11, p. 503], we obtain

$$\left\langle \Lambda_m; \left\langle G_{xx}^A, \mathbf{J}_S \right\rangle'_{S_p} \right\rangle_{S_p} - \left\langle \nabla_t \cdot \Lambda_m, \left\langle G^\phi, \nabla_t' \cdot \mathbf{J}_S \right\rangle'_{S_p} \right\rangle_{S_p} - \left\langle \Lambda_m; \left\langle \underline{\mathbf{G}}^{\text{EM}}, \mathbf{M}_S \right\rangle'_{S_a} \right\rangle_{S_p} = \left\langle \Lambda_m; \mathbf{E}_{t,+}^i \right\rangle_{S_p}, \quad (43)$$

$$\left\langle \Lambda_m; \left\langle \underline{\mathbf{G}}^{\text{HJ}}, \mathbf{J}_S \right\rangle'_{S_p} \right\rangle_{S_a} - \left\langle \Lambda_m; \left\langle G_{xx}^{F+} \mathbf{I}_t + \underline{\mathbf{G}}^{\text{F-}}, \mathbf{M}_S \right\rangle'_{S_a} \right\rangle_{S_a} + \left\langle \nabla_t \cdot \Lambda_m, \left\langle G^{\theta+} + G^{\theta-}, \nabla_t' \cdot \mathbf{M}_S \right\rangle'_{S_a} \right\rangle_{S_a} = \left\langle \Lambda_m; \mathbf{H}_{t,+}^i - \mathbf{H}_{t,-}^i \right\rangle_{S_a}. \quad (44)$$

Here, the incident fields $\mathbf{E}_{t,+}^i$ and $\mathbf{H}_{t,+}^i$ are absent when the waveguide aperture reflection coefficient is calculated, and $\mathbf{H}_{t,-}^i$ is zero in RCS computations.

B. Patch and Aperture Current Expansions

As indicated in Fig. 1, we model the microstrip patch S_p and the aperture S_a using triangular elements. The nodes of a triangular element, whose area is denoted by A , are locally numbered 1, 2, and 3 counterclockwise, as illustrated in Fig. 3. For notational convenience, we introduce the indices, i , j , and k , which assume the values 1, 2, or 3 in a cyclic manner. Hence, referring to Fig. 3, we note that the triangle side opposite node i is formed by the edge vector $\boldsymbol{\ell}_i$ oriented from node j to node k . The position of node i with respect to the global coordinate origin is specified by the vector \mathbf{r}_i , whose projection on the x - y plane is $\boldsymbol{\rho}_i$. Since the microstrip patch and the aperture each lie in a $z = \text{constant}$ plane with z known, the location of an arbitrary point within an element may uniquely be specified by its radial vector $\boldsymbol{\rho} = \boldsymbol{\rho}_i + \boldsymbol{\rho}_i$, where $\boldsymbol{\rho}_i$ is the local position vector originating at node i of the element. As indicated in Fig. 3, the three local position vectors further

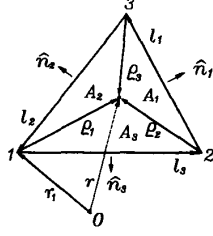


Fig. 3. Local coordinates associated with a triangular element.

divide the element into three triangles, where the area of the triangle opposite node i is denoted by A_i . To facilitate the integration over triangular domains, encountered in (43)–(44), we introduce for each triangle a “natural” coordinate system (L_1, L_2, L_3) , where L_i is known as the *area coordinate* or *shape function* associated with node i of the element [12, p. 110], and is defined as

$$L_i = \frac{A_i}{A}, \quad \sum_{i=1}^3 L_i = 1. \quad (45)$$

In terms of the area coordinates, the local position vector ρ_i may be expressed as

$$\rho_i = \ell_k L_j - \ell_j L_k. \quad (46)$$

To represent the patch and aperture currents on each triangular element, we use vector basis functions given as [13]

$$\Lambda_i = \frac{\rho_i}{2A}. \quad (47)$$

Noting that the gradient of the shape function is

$$\nabla_t L_i = -\hat{n}_i \frac{\ell}{2A} \quad (48)$$

where \hat{n}_i is a unit vector perpendicular to edge i in the plane and pointing out of the triangle element (see Fig. 3), we find the divergence of Λ_i as

$$\nabla_t \cdot \Lambda_i = \frac{1}{A}. \quad (49)$$

We also find that $\hat{n}_i \cdot \Lambda_i$ is constant on edge i , which makes it easy to enforce the continuity of the normal component of current density between the elements that share this edge [13]. The patch current density and its divergence on each element may now be approximated as

$$\mathbf{J}_S = \sum_{i=1}^3 I_i \Lambda_i, \quad \nabla_t \cdot \mathbf{J}_S = \sum_{i=1}^3 \frac{I_i}{A} \quad (50)$$

where I_i is the current leaving the element through edge i . Similarly, the aperture magnetic current density and its divergence on each element are approximated as

$$\mathbf{M}_S = \sum_{i=1}^3 K_i \Lambda_i, \quad \nabla_t \cdot \mathbf{M}_S = \sum_{i=1}^3 \frac{K_i}{A} \quad (51)$$

where K_i is the magnetic current leaving the element through edge i .

C. Global System Assembly and Solution Procedure

The testing functions in the integral equations (43) and (44) are drawn from the same sets as the basis functions used to represent the patch and aperture currents. Hence, $\{\Lambda_m\}$ consists of $\Lambda_i^{(n)}$, with $i = 1, 2$, and 3 , and $n = 1, \dots, N_s$, where N_s is the total number of triangular elements of S_p and S_a . In the above, it was necessary to introduce the superscript n to distinguish the local basis functions associated with element n . In what follows, where there is no danger of confusion, this element superscript will be omitted for notational simplicity.

When the expansions (50) and (51) are substituted into the integral equations (43) and (44), the coefficients $\{I_i^{(n)}\}$ and $\{K_i^{(n)}\}$ are constrained by the boundary conditions, which require the continuity of the normal components of \mathbf{J}_S and \mathbf{M}_S across the edges shared by adjacent elements, or their vanishing at the boundary edges of S_p and S_a , respectively. If the numbers of the nonboundary triangle element edges on the patch and the aperture are denoted by N_p and N_a , respectively, and the total number of the unknown current expansion coefficients by N , then $N = N_p + N_a$. As a result of this procedure, the coupled integral equations (43) and (44) are converted into an algebraic system

$$\begin{bmatrix} [Z_{mn}] & [T_{mn}] \\ [D_{mn}] & [Y_{mn}] \end{bmatrix} \begin{bmatrix} [I_n] \\ [K_n] \end{bmatrix} = \begin{bmatrix} [V_m] \\ [\Pi_m] \end{bmatrix}. \quad (52)$$

Here, the $N \times N$ system matrix consists of four submatrices, where $[Z_{mn}]$ is the $N_p \times N_p$ global impedance matrix, $[T_{mn}]$ is the $N_p \times N_a$ global coupling matrix, $[D_{mn}] = -[T_{mn}]^T$, where the superscript T indicates the matrix transpose, and $[Y_{mn}]$ is the $N_a \times N_a$ global admittance matrix. The $N \times 1$ vector of the unknown current expansion coefficients in (52) comprises the $N_p \times 1$ global vector $[I_n]$ of patch current coefficients and the $N_a \times 1$ global vector $[K_n]$ of aperture current coefficients. The $N \times 1$ global excitation vector consists of the $N_p \times 1$ global patch voltage excitation vector $[V_m]$ and the $N_a \times 1$ global aperture current excitation vector $[\Pi_m]$.

To assemble the global system (52), we consider one source element-test element pair at a time. Each such pair will in general contribute to nine elements of the global system matrix. It is convenient to view these contributions as the entries of a local 3×3 system matrix corresponding to the element pair. Furthermore, each element will in general contribute to three entries of the global excitation vector, and these contributions may be assembled into a local 3×1 excitation vector. To be more specific, let the global indices of the source and test elements be n and m , respectively. Also, suppose that both elements are on the microstrip patch. Then, the associated local system will take the form

$$[Z_{ii'}^{(mn)}] [I_{i'}^{(n)}] = [V_i^{(m)}] \quad (53)$$

where $[Z_{ii'}^{(mn)}]$ is the local impedance matrix, $[I_{i'}^{(n)}]$ is the local vector of current coefficients, and $[V_i^{(m)}]$ is the local voltage excitation vector. Here, the primed local source element indices i' , j' , and k' follow the same cyclic convention

as the unprimed ones. Observe that there exists a unique mapping between the local coefficients $\{I_i^{(n)}\}$ of each element and the global current coefficients $\{I_n\}$, where the reference directions of the latter are specified by the order in which the element nodes appear in the input geometry data. This mapping determines to which entries of the global system (52) the elements of (53) should be added, and with what signs. Local systems similar to (53) arise when both the source and test elements are in the aperture, and when one of them is on the patch and the other in the aperture. Below, we describe these local systems in more detail.

Consider first a test element S_p^m on the patch. Then, if the source element S_p^n is also on the patch, the entries of the resulting local impedance matrix are found as

$$Z_{ii'}^{(mn)} = \left\langle \mathbf{A}_i; \left\langle G_{xx}^A, \mathbf{A}_{i'} \right\rangle'_{S_p^n} \right\rangle_{S_p^m} - \left\langle \frac{1}{A}, \left\langle G^\phi, \frac{1}{A} \right\rangle'_{S_p^n} \right\rangle_{S_p^m}. \quad (54)$$

If, on the other hand, the source element S_a^n is in the aperture, there results a local coupling matrix, with the entries given as

$$T_{ii'}^{(mn)} = \left\langle \mathbf{A}_i; \left\langle \underline{\mathbf{G}}_t^{\text{EM}}, \mathbf{A}_{i'} \right\rangle'_{S_a^n} \right\rangle_{S_p^m}. \quad (55)$$

Each patch element also contributes a local voltage excitation vector, whose entries are

$$V_i^{(m)} = \left\langle \mathbf{A}_i; \mathbf{E}_{t,+}^i \right\rangle_{S_p^m}. \quad (56)$$

Next, consider a test element S_a^m in the aperture. Then, if the source element S_p^n is on the patch, there arises a local coupling matrix, which may be shown (from reciprocity considerations [7, pp. 116–120]) to be the negative transpose of the coupling matrix given by (55). If, on the other hand, the source element S_a^n is also in the aperture, there arises a local admittance matrix, whose entries are given as

$$Y_{ii'}^{(mn)} = Y_{ii',+}^{(mn)} + Y_{ii',-}^{(mn)} \quad (57)$$

where

$$Y_{ii',+}^{(mn)} = \left\langle \mathbf{A}_i; \left\langle G_{xx}^{F+}, \mathbf{A}_{i'} \right\rangle'_{S_a^n} \right\rangle_{S_a^m} - \left\langle \frac{1}{A}, \left\langle G^{\phi+}, \frac{1}{A} \right\rangle'_{S_a^n} \right\rangle_{S_a^m} \quad (58)$$

$$Y_{ii',-}^{(mn)} = \left\langle \mathbf{A}_i; \left\langle \underline{\mathbf{G}}_t^{F-}, \mathbf{A}_{i'} \right\rangle'_{S_a^n} \right\rangle_{S_a^m} - \left\langle \frac{1}{A}, \left\langle G^{\phi-}, \frac{1}{A} \right\rangle'_{S_a^n} \right\rangle_{S_a^m} \quad (59)$$

Finally, each aperture element also contributes a local current excitation vector, with the entries

$$\Pi_i^{(m)} = \left\langle \mathbf{A}_i; \mathbf{H}_{t,+}^i - \mathbf{H}_{t,-}^i \right\rangle_{S_a^m}. \quad (60)$$

The integrals over source coordinates in (54) and (58)–(59) involve kernels that are singular when the test and source elements coincide. These singularities are extracted and integrated analytically [14], leaving well-behaved integrals over

triangular elements, which are then numerically evaluated by a Gaussian quadrature [12, p. 113]. On the other hand, the testing (exterior) integrals in (54) and (58)–(59), as well as the integrals in the excitation terms (56) and (60), have regular and slowly varying integrands, and may thus be approximated using a one-point quadrature rule [13]. For example, the integral in (54) is approximated as

$$\left\langle \mathbf{A}_i; \left\langle G_{xx}^A, \mathbf{A}_{i'} \right\rangle'_{S_p^n} \right\rangle_{S_p^m} \approx \frac{\rho_{ci}^{(m)}}{2} \cdot \left\langle G_{xx}^A(\mathbf{r}_c^{(m)} | \mathbf{r}'), \mathbf{A}_{i'}(\boldsymbol{\rho}') \right\rangle'_{S_p^n} \quad (61)$$

where $\rho_{ci}^{(m)}$ and $\mathbf{r}_c^{(m)}$ denote, respectively, the local (with respect to node i —see Fig. 3) and global position vectors of the centroid of element S_p^m . This one-point approximation results in significant savings in the computational effort, even though it sacrifices the symmetry properties of the impedance and admittance matrices. The integrals appearing in (55) have regular but rapidly varying kernels (which represent electric field, rather than potentials), especially when the substrate between the microstrip patch and the aperture is electrically thin. For this reason, both the interior and exterior integrals in (55) are evaluated by Gaussian quadratures without further approximations.

Once the complex-valued matrix equation (52) is assembled and solved, which is accomplished by standard procedures (LU factorization with partial pivoting, followed by a forward and back substitution [12, p. 120]), the current density within each triangular element may be obtained from (50) or (51).

D. Evaluation of Spectral Integrals and Floquet Series

For the solution procedure described above to be practical, the Sommerfeld-type spectral integrals that occur in (15)–(19) and (22)–(23), as well as the Floquet series that appear in (20)–(21) and (24), must be efficiently evaluated. To accomplish this, the Sommerfeld integrals are accelerated by asymptotic integrand subtraction and the method of averages [15]. In addition to these techniques, an interpolation and table look-up scheme is implemented to further reduce the computation time [16]. The integration path is properly deformed to avoid the integrand singularities, which occur on or near the real axis in the k_ρ plane [17].

The Floquet series are accelerated as well, by a combination of the Kummer and Poisson transformations [18]. As a result of this procedure, the original slowly convergent Floquet series is converted into the sum of an accelerated spectral series and an exponentially convergent spatial series. Observe that in (59) these series are integrated against the basis functions over the source and test triangular elements. The source element integrals are introduced inside the spectral sums and evaluated analytically [18, pp. 107–114], thus further accelerating the convergence of these series. The same integrals over the spatial series are evaluated by a Gaussian quadrature using a singularity treatment similar to that mentioned above.

E. Far-Field and RCS Computation

Once the coefficients $\{I_i\}$ and $\{K_i\}$ are found for each element, the current expansions (50) and (51) are substituted

into (40) and (41) to determine the far zone fields. The integrals encountered in (40) and (41) are then recognized as Fourier transforms of the vector basis functions (47), evaluated at $\mathbf{k}_\rho = \mathbf{k}_\rho^o$. In view of (47) and (46), the Fourier transform of Λ_i associated with a triangular element S_n may be expressed as

$$\begin{aligned}\tilde{\Lambda}_i &= \langle \Lambda_i, e^{-j\mathbf{k}_\rho \cdot \boldsymbol{\rho}} \rangle_{S_n} \\ &= \frac{1}{2A} (\ell_k \tilde{L}_j - \ell_j \tilde{L}_k)\end{aligned}\quad (62)$$

where the \tilde{L}_i denotes the Fourier transformed shape function L_i . Upon using the procedure of Appendix II, we may express \tilde{L}_i as

$$\begin{aligned}\tilde{L}_i &= -\frac{b_i}{2Ak_\rho^2} \sum_{\nu=1}^3 b_\nu j_0(a_\nu k_\rho/2) e^{-j\mathbf{k}_\rho \cdot \boldsymbol{\rho}_{c\nu}} \\ &+ \frac{b_j}{2k_\rho} [j_1(a_j k_\rho/2) - j j_0(a_j k_\rho/2)] e^{j\mathbf{k}_\rho \cdot \boldsymbol{\rho}_{cj}} \\ &- \frac{b_k}{2k_\rho} [j_1(a_k k_\rho/2) + j j_0(a_k k_\rho/2)] e^{j\mathbf{k}_\rho \cdot \boldsymbol{\rho}_{ck}}\end{aligned}\quad (63)$$

where $\boldsymbol{\rho}_{ci}$ is a position vector of the midpoint of edge i of the element, $a_i = \hat{\mathbf{u}} \cdot \boldsymbol{\ell}_i$, $b_i = \hat{\mathbf{v}} \cdot \boldsymbol{\ell}_i$, and j_n denotes the spherical Bessel function of order n . We note that (63) is evaluated for $\mathbf{k}_\rho = \mathbf{k}_\rho^o$, as is required in (40) and (41), then $k_\rho = k_\rho^o$, $\hat{\mathbf{u}} = \hat{\boldsymbol{\rho}}_o$, and $\hat{\mathbf{v}} = \hat{\boldsymbol{\varphi}}_o$. It can be shown that (63) approaches a finite limit $A/3$ as $k_\rho \rightarrow 0$.

Once the microstrip patch and the waveguide aperture contributions to the far zone fields are determined, the RCS is readily obtained from (42).

IV. SAMPLE RESULTS

Although no published results were available for comparison for waveguide-backed microstrip patch antennas, every effort was made to validate at least the most important modules of the developed computer code against independently obtained data. First, the part of the program that deals with an arbitrarily shaped microstrip patch on a grounded substrate (in the absence of the aperture) was extracted and used to compute the scattering characteristics for rectangular patch antennas on both isotropic and uniaxial substrates. The computed RCS results were found to closely agree with those published by Newman and Forrai [17] and Pozar [19]. Second, the part of the code that deals with the aperture was isolated and used to compute the RCS of a narrow slot in a ground plane. This problem was then related via the Babinet's principle [20, p. 500] to that of a thin-wire scatterer with equivalent radius [21], and the latter was analyzed using the commercial code PCAAD [22]. Again, close agreement between the corresponding RCS results was observed. Third, a stripped-down version of our program, which did not include the microstrip patch part, was used to analyze a rectangular waveguide radiating through a centered rectangular slot into a half-space. The computed equivalent magnetic current in the aperture was found to closely agree (both in magnitude and phase) with that obtained by Harrington and Mautz [23, Fig. 15(a)]. Finally, a rectangular waveguide radiating through a centered rectangular aperture covered by a dielectric layer was

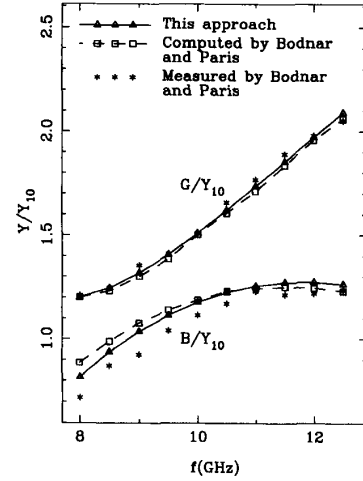


Fig. 4. Aperture conductance G and susceptance B , normalized to the dominant mode wave admittance of a flanged rectangular waveguide radiating through a centered rectangular aperture covered by a lossless isotropic slab with the relative dielectric constant $\epsilon = 2.25$ and thickness $h = 3.201$ mm. The waveguide has dimensions $a = 22.86$ mm and $b = 10.16$ mm, and the aperture size is $0.7a \times 0.8b$.

analyzed. For this problem, in Fig. 4 we compare our aperture admittance results with the computed and measured data obtained by Bodnar and Paris [24]. Although the agreement between the three sets of results is judged to be good, we note that our data are closer to the measured results than the data computed by Bodnar and Paris.

To obtain experimental results, several waveguide-fed microstrip patch antennas were constructed and their characteristics measured. The experiment was done in X -band, rather than in the millimeter-wave range, to reduce the effect of fabrication tolerances on the results. The main components of the measured structure are shown in Fig. 5. Rectangular and circular microstrip patch antennas, with or without a cover layer, were investigated, each excited through a waveguide-backed concentric rectangular slot, as illustrated in Fig. 6(a) and (b), respectively. The substrate and superstrate materials used in the experiment were nonmagnetic and isotropic. Therefore, the n th material layer was characterized by a complex number $\epsilon_n(1 - j \tan \delta_n)$, where ϵ_n and $\tan \delta_n$ denote the real relative dielectric constant and the loss tangent, respectively. The substrate used in antennas of Fig. 6 had $\epsilon_1 = 2.2$, $\tan \delta_1 = 0.001$, and thickness $h = 3.15$ mm. The cover layer, when present, was made of the same material, with thickness $t = 1.57$ mm. The microstrip antennas were mounted on the waveguide flange using plastic screws. The dominant mode reflection coefficient Γ , referred to the aperture plane, was measured using the HP-8510B network analyzer. Prior to the measurement, the thru-reflect-line (TRL) two-port calibration method [25] was used to eliminate the systematic errors due to the coax-to-waveguide adapter and to establish the measurement reference plane at the aperture location.

The measured and computed characteristics of four waveguide-fed microstrip patch antennas are collected for easy reference in Table I. Antennas 1 and 3 are rectangular,

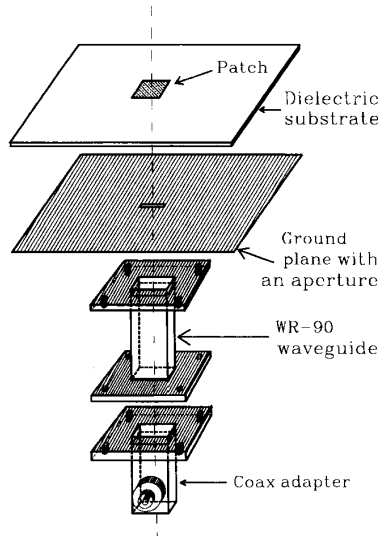


Fig. 5. Components of the measured structure.

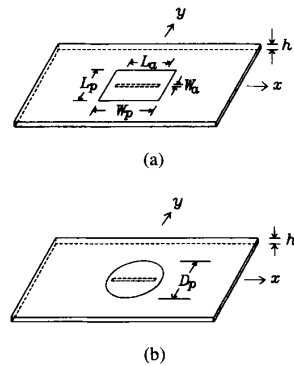


Fig. 6. (a) Rectangular and (b) circular microstrip patch antennas used in the measurements. Each antenna is fed through a waveguide-backed concentric rectangular slot in the ground plane. The dimensions are: $L_p = 11.7$ mm, $W_p = 14.0$ mm, $W_a = .3$ mm, $L_a = 14.0$ mm, $D_p = 14.0$ mm, $h = 3.15$ mm.

as illustrated in Fig. 6(a), while Antennas 2 and 4 are circular, as shown in Fig. 6(b). Antennas 3 and 4 are identical to Antennas 1 and 2, respectively, except that they have a dielectric cover layer. In all cases the same X-band rectangular waveguide (WR-90) was used, with the interior dimensions of $a = 22.86$ mm and $b = 10.16$ mm. Referring to Table I, observe that the largest discrepancy between the computed and measured values of the resonant frequency (f_r), defined as the frequency where the minimum of the voltage standing wave ratio (VSWR) occurs, is less than 1%. Note also that the resonant values of VSWR are close to 1 and, therefore, the antennas are nearly matched at their resonant frequencies. Their bandwidths, however, are narrow (which is characteristic of slot excited microstrip antennas) and do not exceed 5%. Here, the bandwidth (BW) refers to the frequency range around f_r , for which $\text{VSWR} < 2$.

The computed and measured VSWR and phase of the dominant mode reflection coefficient ($\angle\Gamma$) at the slot for

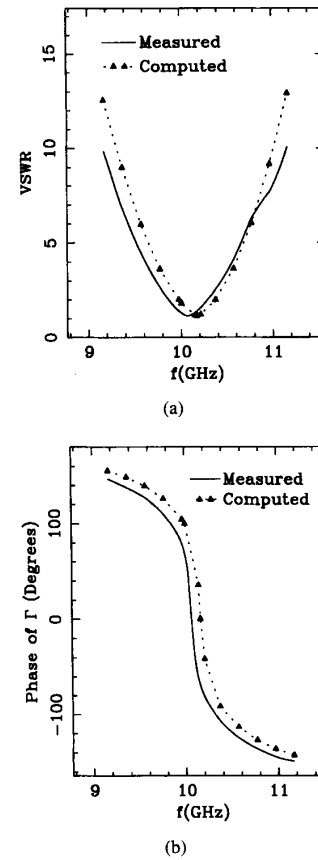


Fig. 7. Plots of (a) VSWR and (b) phase of Γ for a waveguide-excited rectangular patch Antenna 1.

Antennas 1 and 2 of Table I are compared in Figs. 7 and 8, respectively. Similar results were also obtained for Antennas 3 and 4, but are not included due to lack of space. In Fig. 9 we show plots of the computed electric patch current and magnetic slot current for Antenna 1 at the resonant frequency. Since these currents are complex valued, only the dominant part (real or imaginary, as the case may be) is shown in each case. This figure also illustrates the triangular mesh model used in the analysis of Antenna 1. The rectangular patch of Antenna 1 and the circular patch of Antenna 2 were approximated by, respectively, 288 and 394 triangular elements. In both cases the slot was modeled by 44 elements. For Antenna 1, this resulted in a 451×451 global system matrix in (52), and a computation time of approximately 15 min per frequency point on a 12-MIPS computer.

In Fig. 10 we show the measured and computed far-field patterns for Antenna 1. The patterns for Antennas 2–4 are similar and are not included here in the interest of conserving space. The scallop observed in the measured E -plane pattern is almost certainly caused by the surface wave diffraction at the edges of the finite-size ground plane [26]. This effect is more pronounced in the patterns of Antennas 3 and 4 (not shown), because the superstrate increases the intensity of the excited surface wave [4, p. 3].

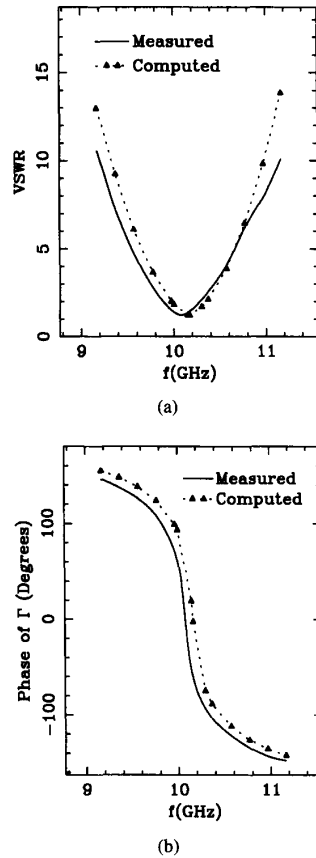


Fig. 8. Plots of (a) VSWR and (b) phase of Γ for a waveguide-excited circular patch Antenna 2.

Next, we present sample results for plane wave excitation. In Fig. 11 we plot versus frequency the magnitude of the dominant mode aperture transmission coefficient T , defined in (39), for Antenna 1. As expected, the peak of transmission occurs at the resonant frequency of the waveguide-driven antenna (see Table I). In Figs. 12 and 13 we plot versus frequency the monostatic RCS of Antennas 1 and 2, respectively, referred to 1 m^2 (the units are decibels above a square meter (dBsm) [27, p. 160]), for a θ -polarized incident plane wave with $E_{\theta}^{\text{inc}} = 1 \text{ V/m}$. In addition to the total RCS, we also plot in Figs. 12–13 the RCS contributions from the microstrip patch and the slot. We note that the slot doesn't influence the first RCS peak of the patch, but it noticeably decreases the second peak. Also, in the case of Fig. 12, the destructive interference between the far fields of the patch and the slot results in an RCS null at approximately 11.1 GHz.

Although the sample results presented above are for antennas operating in X-band, the developed computer code can, of course, be used to design antennas for other frequency bands, including the millimeter-wave range. As an example, consider the waveguide-fed rectangular patch antenna investigated by Kanda *et al.* [5], with the parameters $L_p = 1.25 \text{ mm}$, $W_p = 1.5 \text{ mm}$, $L_a = .862 \text{ mm}$, $W_a = .8862 \text{ mm}$, $h = 0.127 \text{ mm}$, $\epsilon_1 = 2.2$, $\tan \delta_1 = 0.001$ (there was no cover layer), and

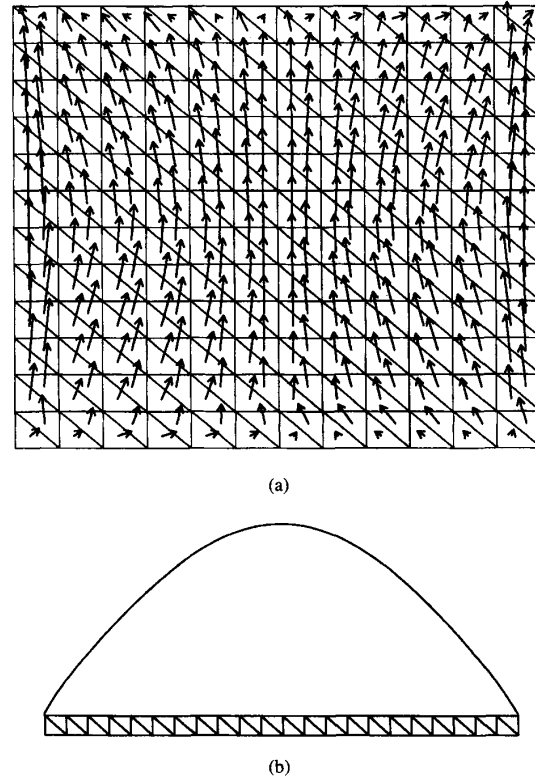


Fig. 9. Resonant currents of Antenna 1. (a) Patch electric current (imaginary part). (b) Slot magnetic current (real part of the longitudinal component).

TABLE I
MEASURED AND COMPUTED CHARACTERISTICS OF
FOUR WAVEGUIDE-FED MICROSTRIP ANTENNAS

Antenna	w/o cover		w/cover	
	1	2	3	4
Measured f_r (GHz)	10.07	10.09	9.73	9.74
Computed f_r (GHz)	10.17	10.17	9.81	9.825
Errors in f_r (%)	0.99	0.79	0.82	0.87
Measured gain (dB)	8.8	8.63	8.54	8.1
Measured VSWR ($f = f_r$)	1.137	1.22	1.023	1.092
Computed VSWR ($f = f_r$)	1.151	1.23	1.055	1.106
Errors in VSWR (%)	1.23	0.82	3.13	1.28
Measured BW (%)	4.24	4.0	4.75	4.6
Computed BW (%)	4.03	3.8	4.27	4.15

the waveguide inner dimensions of $a = 3.78 \text{ mm}$, $b = 1.89 \text{ mm}$. The resonant frequency of this antenna was $f_r = 63.2 \text{ GHz}$ and the minimum VSWR = 5.24. By using our computer code, we have found that this antenna will be matched if the patch and slot dimensions are changed to $L_p = 2.33 \text{ mm}$, $W_p = 3.6 \text{ mm}$, $L_a = 3.6 \text{ mm}$, and $W_a = 0.05 \text{ mm}$. However, with this thin substrate, the bandwidth was less than 1%. When the substrate thickness was increased to $h = 0.525 \text{ mm}$, a 4%

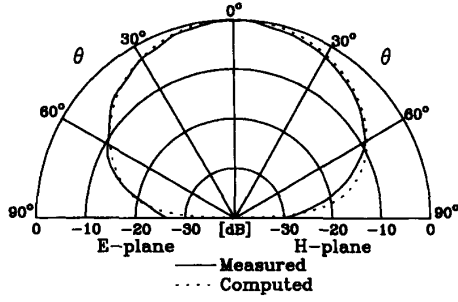


Fig. 10. Measured and computed far-field patterns for Antenna 1.

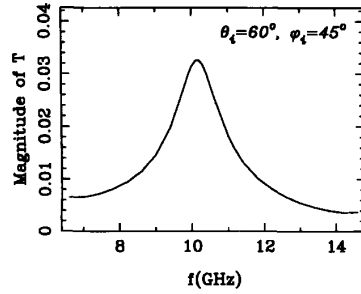


Fig. 11. Magnitude of the dominant mode slot transmission coefficient for Antenna 1.

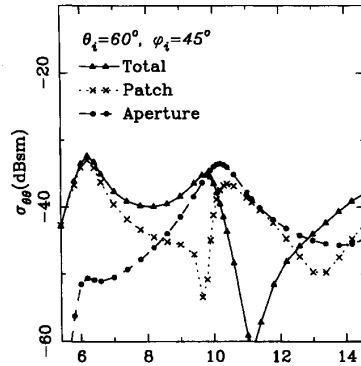


Fig. 12. Monostatic RCS of Antenna 1.

bandwidth was predicted (with slightly modified patch and slot dimensions).

V. SUMMARY AND CONCLUSION

We have presented a rigorous integral equation analysis of a microstrip patch antenna excited through an aperture in the mouth of a rectangular waveguide, or illuminated by a plane wave. The substrate and superstrate may comprise any number of isotropic or uniaxial material layers. The patch and the aperture may both be of arbitrary shape. Hence, using the approach developed here, waveguide-fed microstrip patch antennas of various, possibly irregular shapes, residing in multilayer, isotropic or uniaxial media, may be analyzed within a single formulation, using the same computer program. The

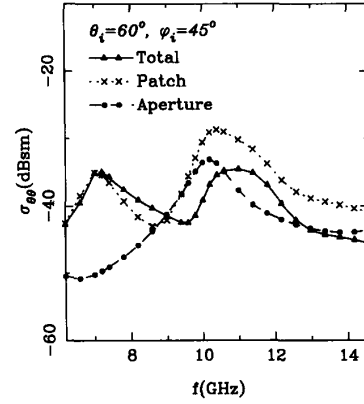


Fig. 13. Monostatic RCS of Antenna 2.

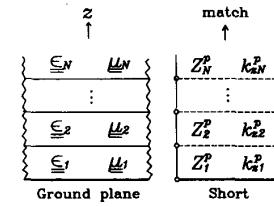


Fig. 14. Layered dielectric medium and its transmission-line network analogue.

analysis has been validated against experimental and published data. We have also shown that the dimensions of the patch and the slot can be selected so that a good impedance match is achieved in this antenna configuration, but only in a narrow frequency band.

APPENDIX I:

TRANSMISSION-LINE ANALOG OF LAYERED MEDIUM

In deriving the integral equations of Section II, we have employed a transmission-line network analog of the layered medium, in which each layer is represented by a transmission line section as illustrated in Fig. 14. This analog comprises two networks that arise from the decomposition of the electromagnetic field into two partial fields that are transverse magnetic (TM) and transverse electric (TE) to z . The quantities corresponding to these networks are distinguished by the superscripts e and h , respectively. The characteristic impedance and propagation constant of the n th section of the TE and TM transmission lines are given as

$$Z_n^e = \frac{1}{Y_n^e} = \frac{k_o \epsilon_{tn}}{\eta_o k_{zn}^e}, \quad Z_n^h = \frac{1}{Y_n^h} = \frac{k_{zn}^h}{\mu_{tn} \eta_o k_o} \quad (64)$$

and

$$k_{zn}^p = \sqrt{k_o^2 \epsilon_{tn} \mu_{tn} - k_p^2} \quad (65)$$

where the superscript p stands for e or h .

Let the network be excited by a 1-A shunt current source located at z' in the n th line section of length d_n , as illustrated in Fig. 15(a). Then, the voltage $V_i(z | z')$ and current $I_i(z | z')$

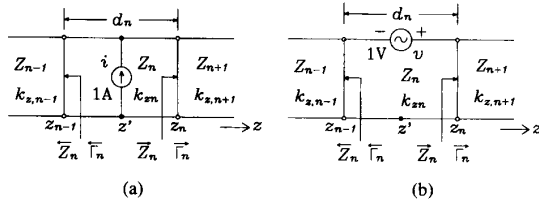


Fig. 15. Typical transmission line section with (a) 1-A shunt current source and (b) 1-V series voltage source.

at a point z within this line section obey the equations [28, p. 747]:

$$\frac{d}{dz} V_i(z | z') = -jk_{zn} Z_n I_i(z | z') \quad (66)$$

$$\frac{d}{dz} I_i(z | z') = -jk_{zn} Y_n V_i(z | z') + \delta(z - z') \quad (67)$$

where δ denotes the delta function. Here and below, we omit the superscript p for notational simplicity. From (66) and (67), $V_i(z | z')$ may be expressed in the traveling-wave form

$$V_i(z | z') = \frac{e^{-jk_{zn}|z-z'|}}{2Y_n [1 - \bar{\Gamma}_n(z_o) \bar{\Gamma}_n(z_o)]} \cdot \left[1 + \bar{\Gamma}_n(z_o) e^{-j2k_{zn}(z < -z_o)} \right] \times \left[1 + \bar{\Gamma}_n(z_o) e^{-j2k_{zn}(z > -z_o)} \right] \quad (68)$$

where $z_< \equiv \min(z, z')$, $z_> \equiv \max(z, z')$, and $\bar{\Gamma}_n(z_o)$ and $\bar{\Gamma}_n(z_o)$ are the reflection coefficients *looking to the left* and *looking to the right*, respectively, at any location z_o within the line section. By means of the translation formula

$$\bar{\Gamma}_n(z) = \bar{\Gamma}_n(z_o) e^{\pm j2k_{zn}(z - z_o)} \quad (69)$$

where the right and left arrows correspond to the upper and lower signs, respectively, these reflection coefficients can always be expressed in terms of the terminal reflection coefficients, $\bar{\Gamma}_n$ and $\bar{\Gamma}_n$, which are related to the corresponding terminal impedances \bar{Z}_n and \bar{Z}_n as

$$\bar{\Gamma}_n = \frac{\bar{Z}_n - Z_n}{\bar{Z}_n + Z_n} \quad (70)$$

The voltage $V_v(z | z')$ and current $I_v(z | z')$ excited by a 1-V series voltage source v in the n th line section, as illustrated in Fig. 15(b), satisfy equations dual to (66) and (67), which are obtained from the latter by making the substitutions $V_i \rightarrow I_v$, $I_i \rightarrow V_v$, $Z_n \rightarrow Y_n$, and $Y_n \rightarrow Z_n$. Furthermore, it can be shown that the following symmetry and reciprocity relations hold (see [28, p. 194]):

$$V_i(z | z') = V_i(z' | z), I_v(z | z') = I_v(z' | z), \\ V_v(z | z') = -I_i(z' | z). \quad (71)$$

As a result, $I_v(z | z')$ can be obtained from (68) by replacing Y_n in the latter with Z_n (which also causes the reflection coefficients to change signs). $I_i(z | z')$ follows from (66)

and (68), and $V_v(z | z')$ may then be obtained from the last relation in (71).

The voltage and current on the n th transmission line section that is source-free satisfy the homogeneous form of (66)–(68). From these equations, the voltage at any point z within the same line section may be found as

$$V(z) = V(z_o) \frac{e^{\mp jk_{zn}(z - z_o)}}{1 + \bar{\Gamma}_n(z_o)} \left[1 + \bar{\Gamma}_n(z_o) e^{\pm jk_{zn}(z - z_o)} \right] \quad (72)$$

where the upper (lower) sign corresponds to $z > z_o$ ($z < z_o$). In the above, $z_o = z_n$ or $z_o = z_{n+1}$, depending on whether the source is located to the left or right, respectively, of the line section, and $V(z_o)$ is the voltage across the line terminals at $z = z_o$. We have omitted the subscript of V in (72), because the latter applies irrespective of the nature of the source, and have dropped z' from its argument because (72) only implicitly depends on the source location, which is outside the line section. The current $I(z)$ corresponding to (72) may be obtained by substituting the latter into (66).

VII. APPENDIX II:

FOURIER TRANSFORM OF A TRIANGLE SHAPE FUNCTION

The Fourier transform of a shape function L_i associated with the n th triangular element is given as

$$\tilde{L}_i = \int_{S_n} L_i e^{j\mathbf{k}_\rho \cdot \boldsymbol{\rho}} dS \quad (73)$$

where $\mathbf{k}_\rho = \hat{\mathbf{u}} k_\rho$. To evaluate the integral in (73), it is helpful to first convert it to a line integral around the boundary contour, ∂S_n , of S_n (see [29]–[31]). This is most easily accomplished by noting that

$$e^{j\mathbf{k}_\rho \cdot \boldsymbol{\rho}} = \nabla_t \cdot \left(\hat{\mathbf{u}} \frac{e^{j\mathbf{k}_\rho \cdot \boldsymbol{\rho}}}{jk_\rho} \right) \quad (74)$$

and by making use of the divergence theorem. As a result, when $k_\rho \neq 0$, we obtain

$$\tilde{L}_i = \frac{1}{2Ak_\rho^2} \oint_{\partial S_n} (2jk_\rho AL_i + \hat{\mathbf{v}} \cdot \boldsymbol{\ell}_i) e^{j\mathbf{k}_\rho \cdot \boldsymbol{\rho}} \hat{\mathbf{u}} \cdot \hat{\mathbf{n}} d\ell \quad (75)$$

where $\hat{\mathbf{v}} = \hat{\mathbf{z}} \times \hat{\mathbf{u}}$ and $\hat{\mathbf{n}}$ denotes a unit vector normal to ∂S_n at ℓ in the plane and pointing out of S_n . The integral in (75) is easily evaluated in the local coordinates if one notes that when ℓ is on edge i , $\hat{\mathbf{n}} = \hat{\mathbf{n}}_i$, $0 \leq L_k \leq 1$, $L_i = 0$, $L_j = 1 - L_k$, and $d\ell = \ell_i dL_k$ (see Fig. 3). Also, in that case $\boldsymbol{\rho} = \boldsymbol{\rho}_j + \boldsymbol{\rho}_j$, where $\boldsymbol{\rho}_j$ is a vector from node j to the point ℓ on edge i of the element. The resulting closed-form expression for \tilde{L}_i is given in (63).

ACKNOWLEDGMENT

The authors thank Dr. C.-I. G. Hsu for many valuable discussions and to F. Lu, J. Navarro, and M.-Y. Li for their assistance in the experiment.

REFERENCES

- [1] I. J. Bahl and P. Bhartia, *Microstrip Antennas*. Dedham, MA: Artech, 1980.
- [2] J. R. James, P. S. Hall, and C. Wood, *Microstrip Antenna Theory and Design*. London: Peter Peregrinus, 1981.
- [3] K. Chang, "Millimeter-wave planar integrated circuits and subsystems," in *Millimeter Components and Techniques, Part V—Infrared and Millimeter Waves*, K. J. Button, Ed. New York: Academic, 1985, vol. 14, pp. 79–187.
- [4] P. Bhartia, K. V. S. Rao, and R. S. Tomar, *Millimeter-Wave Microstrip and Printed Circuit Antennas*. Norwood, MA: Artech, 1991.
- [5] M. Kanda, D. C. Chang, and D. H. Greenlee, "The characteristics of iris-fed millimeter-wave rectangular microstrip patch antennas," *IEEE Trans. Electromagn. Comput.*, vol. EMC-27, pp. 212–220, Nov. 1985.
- [6] K. C. Gupta, R. Garg, and R. Chadha, *Computer-Aided Design of Microwave Circuits*. Norwood, MA: Artech, 1981.
- [7] R. F. Harrington, *Time-Harmonic Electromagnetic Field*. New York: McGraw-Hill, 1961.
- [8] C. M. Butler, Y. Rahmat-Samii, and R. Mittra, "Electromagnetic penetration through apertures in conducting surfaces," *IEEE Trans. Antennas Propagat.*, vol. AP-26, pp. 82–93, Jan. 1978.
- [9] K. A. Michalski and D. Zheng, "Integral equation analysis of arbitrarily shaped microstrip structures," Tech. Rep. for ONR, Contract N00014-90-J-1197, Dept. of Electrical Engineering, Texas A & M Univ., Apr. 1990.
- [10] V. Teodoridis, T. Sphicopoulos, and F. Gardiol, "The reflection from an open-ended rectangular waveguide terminated by a layered dielectric medium," *IEEE Trans. Microwave Theory Tech.*, vol. MTT-33, pp. 359–366, May 1985.
- [11] J. Van Bladel, *Electromagnetic Fields*. New York: Hemisphere, 1985.
- [12] L. Lapidus and G. F. Pinder, *Numerical Solution of Partial Differential Equations in Science and Engineering*. New York: Wiley, 1982.
- [13] S. M. Rao, D. R. Wilton, and A. W. Glisson, "Electromagnetic scattering by surfaces of arbitrary shape," *IEEE Trans. Antennas Propagat.*, vol. AP-30, pp. 409–418, May 1982.
- [14] D. R. Wilton et al., "Potential integrals for uniform and linear source distributions on polygonal and polyhedral domains," *IEEE Trans. Antennas Propagat.*, vol. AP-32, pp. 276–281, Mar. 1984.
- [15] J. R. Mosig, R. C. Hall, and F. E. Gardiol, "Numerical analysis of microstrip patch antennas," in *Handbook of Microstrip Antennas*, J. R. James and P. S. Hall, Eds. London: Peter Peregrinus, 1989.
- [16] J. R. Mosig and F. E. Gardiol, "A dynamical radiation model for microstrip structures," in *Advanced Electronic Electron Physics*, P. W. Hawkes, Ed. New York: Academic, 1982, vol. 59, pp. 139–237.
- [17] E. H. Newman and D. Forrai, "Scattering from a microstrip patch," *IEEE Trans. Antennas Propagat.*, vol. AP-35, pp. 245–251, Mar. 1987.
- [18] N. W. Montgomery, "Periodic structures in stratified media—a mixed potential formulation," Ph.D. dissertation, Univ. of Houston, Houston, TX, May 1991.
- [19] D. M. Pozar, "Radiation and scattering from a microstrip patch on a uniaxial substrate," *IEEE Trans. Antennas Propagat.*, vol. AP-35, pp. 613–621, June 1987.
- [20] G. T. Ruck, D. E. Barrick, W. D. Stuart, and C. K. Krichbaum, Eds., *Radar Cross Section Handbook*, vol. 2. New York: Plenum, 1970.
- [21] C. M. Butler, "The equivalent radius of a narrow conducting strip," *IEEE Trans. Antennas Propagat.*, vol. AP-30, pp. 755–758, July 1982.
- [22] D. M. Pozar, *Personal Computer Aided Antenna Design*. Leverett, MA: Antenna Design, Dec. 1991.
- [23] R. F. Harrington and J. R. Mautz, "Electromagnetic coupling through apertures by the generalized admittance approach," *Comput. Phys. Commun.*, vol. 68, pp. 19–42, 1990.
- [24] D. G. Bodnar and D. T. Paris, "New variational principle in electromagnetics," *IEEE Trans. Antennas Propagat.*, vol. AP-18, pp. 216–223, Mar. 1970.
- [25] "Network analysis—applying the HP 8510B TRL calibration for non-coaxial measurements," HP Product Note 8510-8, Palo Alto, CA, Oct. 1987.
- [26] S. A. Bokhari, J. R. Mosig, and F. E. Gardiol, "Radiation pattern computation of microstrip antennas on finite size ground planes," *IEE Proc., Pt. H*, pp. 278–286, 1992.
- [27] E. F. Knott, J. F. Shaeffer, and M. T. Tuley, *Radar Cross Section: Its Prediction, Measurement and Reduction*. Norwood, MA: Artech, 1985.
- [28] L. B. Felsen and N. Marcuvitz, *Radiation and Scattering of Waves*. Englewood Cliffs, NJ: Prentice, 1973.
- [29] B. Houshmand, W. C. Chew, and S. W. Lee, "Fourier transform of a linear distribution with triangular support and its applications in electromagnetics," *IEEE Trans. Antennas Propagat.*, vol. 39, pp. 252–254, Feb. 1991.
- [30] K. McInturf and P. S. Simon, "The Fourier transform of linearly varying functions with polygonal support," *IEEE Trans. Antennas Propagat.*, vol. 39, pp. 1441–1443, Sept. 1991.
- [31] T.-S. Horng, N. G. Alexopoulos, S.-C. Wu, and H.-Y. Yang, "Full-wave spectral-domain analysis for open microstrip discontinuities of arbitrary shape including radiation and surface-wave losses," *Int. J. Microwave Millimeter-Wave Comput.-Aided Eng.*, vol. 2, no. 4, pp. 224–240, 1992.



interests include electromagnetics, microwave circuits and numerical methods.



Krzysztof A. Michalski (S'78–M'81–SM'88) received the M.Sc. degree from the Technical University of Wrocław, Poland, in 1974, and the Ph.D. degree from the University of Kentucky, Lexington, in 1981, both in electrical engineering.

He was on the faculty of the University of Mississippi from 1982 to 1986, and in 1987 he joined Texas A&M University as an Associate Professor. His research interests include analytical and numerical methods of electromagnetics.



Kai Chang (S'75–M'76–SM'85–F'91) received the B.S.E.E. degree from the National Taiwan University, Taipei, Taiwan, the M.S. degree from the State University of New York, Stony Brook, and the Ph.D. degree from the University of Michigan, Ann Arbor, in 1970, 1972, and 1976, respectively.

From 1972 to 1976, he worked for the Microwave Solid-State Circuits Group, Cooley Electronics Laboratory of the University of Michigan as a Research Assistant. From 1976 to 1978, he was employed by Shared Applications, Inc., Ann Arbor, where he worked in computer simulation of microwave circuits and microwave tubes. From 1978 to 1981, he worked for the Electron Dynamics Division, Hughes Aircraft Company, Torrance, CA, where he was involved in the research and development of millimeter-wave solid-state devices and circuits, power combiners, oscillators, and transmitters. From 1981 to 1985, he worked for the TRW Electronics and Defense, Redondo Beach, CA, as a Section Head, developing state-of-the-art millimeter-wave integrated circuits and subsystems including mixers, VCO's, transmitters, amplifiers, modulators, upconverters, switches, multipliers, receivers, and transceivers. He joined the Electrical Engineering Department of Texas A&M University in August 1985 as an Associate Professor and was promoted to a Professor in 1988. In January 1990, he was appointed E-Systems Endowed Professor of Electrical Engineering. His current interests are in microwave and millimeter-wave devices and circuits, microwave integrated circuits, microwave optical interactions and antennas.

Dr. Chang served as the editor of the four-volume *Handbook of Microwave and Optical Components* (Wiley, 1989 and 1990). He is the editor of the *Microwave and Optical Technology Letters* and the Wiley Book Series in Microwave and Optical Engineering. He has published over 180 technical papers and several book chapters in the areas of microwave and millimeter-wave devices and circuits. He received the Special Achievement Award from TRW in 1984, the Halliburton Professor Award in 1988, the Distinguished Teaching award in 1989, and the Distinguished Research Award in 1992 from the Texas A&M University.